

Chalcohalide Antiperovskite Thin Films with Visible Light Absorption and High Charge-Carrier Mobility Processed by Solvent-Free and Low-Temperature Methods

Peer-reviewed author version

Sebastia-Luna, Paz; Rodkey, Nathan; Mirza, Adeem Saeed; MERTENS, Sigurd; Lal, Snigdha; Carranza, Axel Melchor Gaona; Calbo, Joaquin; Righetto, Marcello; Sessolo, Michele; Herz, Laura M.; VANDEWAL, Koen; Orti, Enrique; Morales-Masis, Monica; Bolink, Henk J. & Palazon, Francisco (2023) Chalcohalide Antiperovskite Thin Films with Visible Light Absorption and High Charge-Carrier Mobility Processed by Solvent-Free and Low-Temperature Methods. In: CHEMISTRY OF MATERIALS, 35 (16) , p. 6482 -6490.

DOI: 10.1021/acs.chemmater.3c01349

Handle: <http://hdl.handle.net/1942/41638>

Chalcohalide Antiperovskite Thin Films with Visible Light Absorption and High Charge-Carrier Mobility Processed by Solvent-Free and Low-Temperature Methods

Paz Sebastián-Luna,^a Nathan Rodkey,^{a,b} Adeem Saeed Mirza,^b Sigurd Mertens,^c Snigdha Lal,^d Axel M. Gaona-Carranza,^a Joaquín Calbo,^a Marcello Righetto,^d Michele Sessolo,^a Laura M. Herz,^{d,e} Koen Vandewal,^c Enrique Ortí,^a Mónica Morales-Masis,^b Henk J. Bolink,^{a,*} and Francisco Palazon^{a,f*}

^a Instituto de Ciencia Molecular, Universidad de Valencia, 46980 Paterna, Spain

^b MESA+ Institute for Nanotechnology, University of Twente, Enschede 7500 AE, The Netherlands

^c Institute for Materials Research (IMO-IMOMEC), Hasselt University, Diepenbeek BE – 3590, Belgium

^d Department of Physics, University of Oxford, Clarendon Laboratory, Parks Road, Oxford OX1 3PU, UK.

^e Institute for Advanced Study, Technical University of Munich, Lichtenbergstrasse 2a, D-85748 Garching, Germany.

^f Departamento de Ingeniería Química y Ambiental, Universidad Politécnica de Cartagena, 30202 Cartagena, Spain

Chalcohalide, Antiperovskite, Mechanochemical Synthesis, Thin Film, PLD

ABSTRACT: Silver chalcohalide antiperovskites represent a rather unexplored alternative to lead halide perovskites and other semiconductors based on toxic heavy metals. All synthetic approaches reported so far for Ag_3SI and Ag_3SBr require long synthesis times (typically days, weeks or even months) and high temperatures. Herein, we report the synthesis of these materials by a fast and low-temperature method involving mechanochemistry. Structural and optical properties are examined experimentally as well as by density functional theory. Furthermore, we deposit Ag_3SI as thin film by pulsed laser deposition and characterize its optoelectronic properties by optical pump terahertz probe measurements, revealing a high charge-carrier mobility of $49 \text{ cm}^2\text{V}^{-1}\text{s}^{-1}$. This work paves the way to the implementation of chalcohalide antiperovskites in various optoelectronic applications.

1. INTRODUCTION

Lead halide perovskites have marked a revolution in optoelectronics and other energy-related applications in the last decade. Much of the success of these materials can be related to the extraordinary versatility of the perovskite structure which allows for a broad range of related crystal phases (*e.g.*, tetragonal and orthorhombic distortions) and chemical compositions (*e.g.*, multi-cation and/or multi-anion compositions). Yet, beyond lead halide perovskites, there exists a number of analogous compounds, many of which remain relatively underexplored.¹ This is the case of the antiperovskite structure, where “anti” refers to the swapped positions of the anions and cations in the ABX_3 structure (see Figure 1).

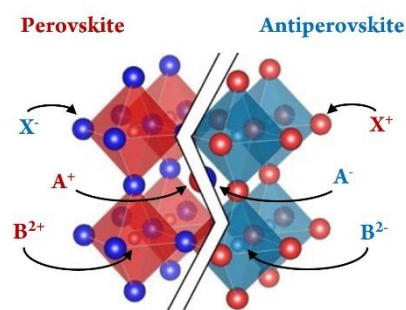


Figure 1. Schematic representation of halide perovskite (left) and chalcohalide antiperovskite (right) crystal structures. The antiperovskite structure can be viewed as a perovskite structure where anions (in red) are replaced by cations (in blue) and viceversa.

As is also true for lead halide perovskites,² chalcohalide antiperovskites are not newly discovered materials. Indeed, Ag_3SI and Ag_3SBr , which adopt the antiperovskite structure, have been reported at least since 1960 (note that these can also be written as ISAg_3 and BrSAg_3 to stress the analogy with the more typical ABX_3 representation of the perovskite structure).³ Nevertheless, the vast majority

of synthesis methods reported so far are carried out in a quartz tube sealed under vacuum and require very high temperatures, often substantially above 200 °C and long synthesis times (see Table 1), which make these processes unsuitable for most applications.

Table 1. Summary of reported synthesis conditions for Ag₃SI and Ag₃SBr. The maximum temperatures achieved during each synthesis and their total time are given.

Material	Maximum temperature (°C)	Total time	References
Ag ₃ SI, Ag ₃ SBr	200	1 month	4,5
Ag ₃ SBr	220	10 days	6
Ag ₃ SI, Ag ₃ SBr	280	2 months	7,8
Ag ₃ SI, Ag ₃ SBr	300	4–5 days	3,9,10
Ag ₃ SBr	300	10 days	11
Ag ₃ SI, Ag ₃ SBr	400	4–5 days	12,13
Ag ₃ SI	550	17 hours	14
Ag ₃ SI, Ag ₃ SBr	550	5–7 days	15–17
Ag ₃ SI	600	1 day	17
Ag ₃ SI	700	3 months	18
Ag ₃ SI	750	3 hours	19
Ag ₃ SI	800	6–7 days	20,21
Ag ₃ SBr	800	6 months	22,23
Ag ₃ SBr	800	1 month	24
Ag ₃ SBr	800	4 months	25
Ag ₃ SI	850	30 hours	26
Ag ₃ SI, Ag ₃ SBr	Digestion - 200	2–3 days	7,26–30

The main interest for these materials so far has been related to their relatively high ion conductivity first reported by Takahashi and Yamamoto in 1966.¹⁴ Most of the later work has been focused on elucidating the crystallography and phase transitions of these antiperovskites. Regarding Ag₃SI, at least 4 polymorphs have been reported usually noted α , α^* , β , and γ which structurally differ in the ordering of the different ions.³¹ The α phase, with disordered S²⁻/I⁻ anions is reported to be the most stable at temperatures above 250 °C. Upon cooling to room temperature, α -

Ag₃SI may convert to the reportedly more stable β phase with ordered anions and lower ionic conductivity, or transform into the metastable α^* phase, which has disordered S²⁻/I⁻ anions (and higher ionic conductivity) as the high-temperature α phase but differs in the position of the Ag⁺ cations. The γ phase, which implies Ag⁺ cation ordering, is only reported at low temperatures (< 128 K).³² Electrical conductivity in all cases has been ascribed mostly to ion movement. Regarding optical properties, Ag₃SI is reported to be a narrow-bandgap semiconductor with theoretically- and experimentally-determined direct bandgaps around 0.9–1.1 eV at room temperature,^{13,33} which make it especially promising for photovoltaics. Ag₃SBr appears to be less studied in comparison with scarce and conflicting bandgap energies reported from 0.3 eV to 1.9 eV.^{34–36} Eventually, regarding the deposition of thin films, we are only aware of one report by Tver'yanovich *et al.*¹⁹ on multilayer films lacking detailed structural and/or elemental analysis.

In summary, silver chalcogenide antiperovskites appear as promising low-toxicity alternatives to lead halide perovskites and other semiconductors for photovoltaics and other optoelectronic applications. Nevertheless, with regards to literature, it is obvious that for the potential implementation of these materials in such fields, it is paramount to be able to obtain the antiperovskites in a much more time- and energy-efficient manner than those described in Table 1. Furthermore, the deposition of relevant thin films remains virtually unexplored. Finally, optoelectronic properties beyond ionic conductivity and especially on thin film samples, are yet to be accurately determined.

Here, we demonstrate that Ag₃SBr and Ag₃SI antiperovskites can be synthesized as non-templated high-purity powders by fast and low-temperature processes combining mechanochemical synthesis and mild thermal annealing. Light-absorption properties of the obtained crystallites are characterized experimentally by photothermal deflection spectroscopy (PDS). Furthermore, Ag₃SI is deposited as thin film by pulsed laser deposition (PLD). Structural, morphological and elemental characterization are carried out by X-ray Diffraction (XRD), scanning electron microscopy (SEM), and energy-dispersive X-ray spectroscopy (EDS) demonstrating the formation of compact antiperovskite thin films with thicknesses in the hundreds of nanometers. Optical characterization including air photoelectron spectroscopy (APS), Kelvin probe measurements (KP), and PDS as well as UV-vis optical absorption are employed to gain some insights into the energy levels of Ag₃SI semiconductor thin films. Optical pump terahertz probe (OTTP) measurements demonstrate for the first time the high charge-carrier mobility for these materials (note that reports on high mobilities so far have focused on ion mobilities which the terahertz probe is largely insensitive to) and reveal that charge carriers are short lived. Eventually, density functional theory (DFT) calculations are undertaken to shed more light into the optoelectronic properties of Ag₃SI and Ag₃SBr antiperovskites as well as on their dependence on structural disorder.

2. RESULTS AND DISCUSSION

2.1. CHEMICAL SYNTHESIS AND STRUCTURAL CHARACTERIZATION OF Ag₃SX POWDERS

Based on our previous work on the mechanochemical synthesis of different metal-halide materials,³⁷ we ball-milled stoichiometric amounts of Ag_2S and AgX ($X = \text{Br}, \text{I}$) for 1 h under inert atmosphere. However, this did not lead to the synthesis of Ag_3SI or Ag_3SBr , as shown in Figure 2a,c. Nevertheless, upon annealing at a moderate temperature of 160 °C for 30 min in nitrogen, Ag_3SI is formed from the ball-milled mixture of Ag_2S and AgI without any noticeable traces of unreacted precursors or by-products, as evidenced by the XRD analysis presented in Figure 2b. In the case of the bromide analogue, small traces of unreacted AgBr are still present when annealing at 160 °C (Figure S1), which vanish completely when heated to 220 °C (Figure 2d).

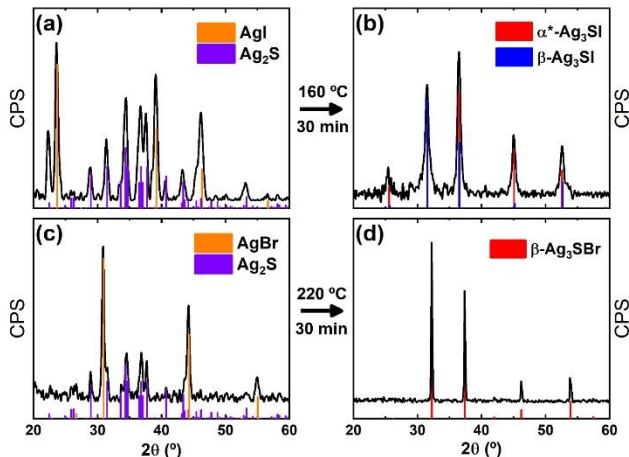


Figure 2. XRD of stoichiometric $\text{AgI}+\text{Ag}_2\text{S}$ (a) and $\text{AgBr}+\text{Ag}_2\text{S}$ (c) mixtures ball-milled for 1 h. XRD of resulting antiperovskite after thermal annealing in nitrogen at 160 °C (b) or 220 °C (d) for 30 min of (a) and (c), respectively. Reference patterns for AgI , AgBr , Ag_2S , $\alpha^*\text{-Ag}_3\text{SI}$, $\beta\text{-Ag}_3\text{SI}$, and $\beta\text{-Ag}_3\text{SBr}$ correspond to Inorganic Crystal Structure Database (ICSD) entries #56552, #56546, #182916, #93429, #202123, and #25531, respectively.

Note that such thermal annealing at low temperature of pristine (non-ball-milled) powder mixtures does not yield the desired antiperovskite phase (see Figures S2 and S3), so that both steps (ball-milling + thermal annealing) are found to be necessary to obtain Ag_3SX . To be more precise on the obtained antiperovskite phases, Rietveld refinement (whose details can be found as Supporting Information in Figure S4 and Table S1) yields a composition of 75% $\alpha^*\text{-Ag}_3\text{SI}$ and 25% $\beta\text{-Ag}_3\text{SI}$ in the case of the iodide compound. In the case of $X = \text{Br}$, according to XRD (Figure S1), $\beta\text{-Ag}_3\text{SBr}$ (cubic antiperovskite; space group $Pm\text{-}3m$) is formed at 220 °C and is stable at room temperature.³² This analysis demonstrates that high-purity, non-templated Ag_3SX ($X = \text{I}$ or Br) antiperovskites can be synthesized by a much faster and lower-temperature route compared to reported protocols in literature (see Table 1).

2.2. VISIBLE AND INFRARED LIGHT ABSORPTION CHARACTERIZATION

Determination of the absorption spectrum of powder samples by conventional transmission and reflection measurements is hampered by light scattering. We there-

fore used photothermal deflection spectroscopy (PDS; Figure 3) to characterize the optical response of Ag_3SX samples in the visible and near-infrared region. PDS measures the (relative) amount of heat produced upon photon absorption.³⁸ If the samples are not very emissive, as is the case here, only a tiny portion of the absorbed energy is re-emitted. Thus, for weakly emissive samples, almost all absorbed energy is converted to heat, resulting in a PDS spectrum proportional to the optical absorption spectrum. Note that, as opposed to transmission and reflection measurements, the PDS measurement is not affected by light scattering and if no absorption takes place, the PDS signal is zero. It is therefore ideally suited to characterize absorption onsets of highly scattering samples, such as powder samples.

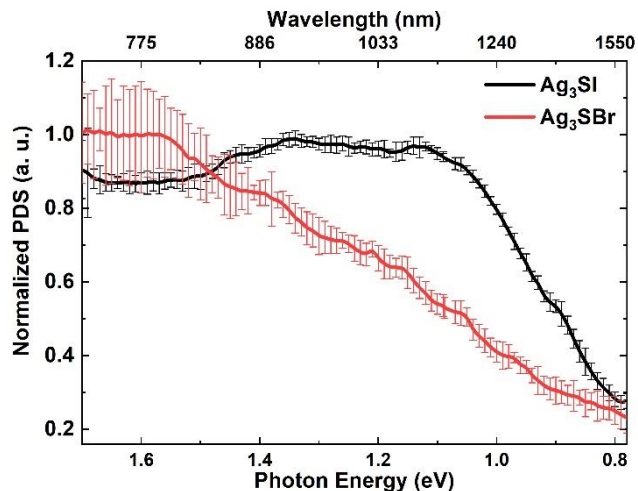


Figure 3. Photothermal deflection spectroscopy (PDS) characterization of Ag_3SI (black) and Ag_3SBr (red) powders. The PDS signal is proportional to the absorption spectrum. Error bars represent 95% confidence intervals.

The most striking feature in view of Figure 3 is the lack of a clear onset in the PDS signal that would allow for a clear determination of the bandgap energy value. This is especially so in the case of Ag_3SBr where a shallow slope is present from 0.8 eV to 1.55 eV. We note however that this spectrum is very similar to previous characterization of the same compound by the closely-related technique of photoacoustic spectroscopy and could be related to sub-bandgap absorption by impurities.³⁶ However, we note as well that similar shallow absorption onsets have also been reported for several multinary semiconductors (*e.g.*, kesterites, ABZ_2 semiconductors), which are attributed to lattice disorder.^{39–41} Here, the disorder in the occupation of lattice sites has been shown to yield Gaussian disorder in the density of states, resulting in broad absorption tails. In any case, moving from $X = \text{Br}$ to $X = \text{I}$ seems to yield a red-shift in absorption similar to that observed on tin and lead halide perovskites, with Ag_3SI showing strong light absorption throughout the visible range as well as near infrared, which makes it promising for light-harvesting applications such as photovoltaics.

2.3. PULSED LASER DEPOSITION OF Ag_3SI THIN FILMS

Given the demonstrated fast and low-temperature synthesis of these silver chalcogenide antiperovskites and their promising properties for optoelectronics, we attempted the deposition of Ag_3SI thin films. Thermal single- and dual-source evaporation, which have proven to be suitable for lead-halide perovskites^{42–44} were investigated with little success. No evidence of sulphur incorporation into the thin films was found, meaning that both the pre-synthesized Ag_3SI (in the single-source evaporation configuration) and Ag_2S (in the dual-source co-evaporation configuration) undergo decomposition and incongruent evaporation or sublimation with loss of sulphur at low temperatures (see Figures S5 and S6). In contrast, antiperovskite thin-films of around 140 nm thickness (Figure 4a) were successfully deposited by pulsed laser deposition (PLD) in a similar manner as recently reported for silver-bismuth-based halide double perovskites.⁴⁵ In brief, Ag_3SI powder is formed, first by mechanochemical synthesis, and then annealed as described in the Supporting Information. These stoichiometric powders are then pressed into a pellet and loaded into a PLD chamber. Ar gas is introduced to reach a working pressure of 1.5×10^{-2} mbar, after which an excimer laser (248 nm) ablates the target at a frequency of 10 Hz. The substrate is kept at room temperature for all depositions.

To begin with, the stoichiometric transfer of material from target to substrate was studied by energy dispersive X-ray spectroscopy (EDX). By tuning the fluence of the excimer laser from 2 J cm^{-2} to 0.3 J cm^{-2} we observe little effect on the incorporation of sulphur into the thin-films, which remain sulphur-poor. Instead, we find that the ratio of Ag:I can be tuned from 3.73 at 2 J cm^{-2} (an iodide deficiency) to 2.07 at 0.75 J cm^{-2} (an iodide excess) (Table S2). A fluence of 0.75 J cm^{-2} was chosen for this work, keeping an iodide excess in the film. This fluence was chosen in part to avoid the nucleation of metallic Ag crystals observed upon annealing of Ag-rich films (Figure S7). The sulphur deficiency was then compensated by adding an excess of elemental sulphur to the antiperovskite powder with a molar ratio of 3:1 before target pressing (see the Supporting Information for more details, Figure S8). Thin-films deposited with these targets were studied by EDX, and a sulphur excess was observed (Table 2). Samples were then annealed at 200°C for 30 minutes in a nitrogen atmosphere, and then measured once again by EDX. After this annealing process, the ratios of Ag:I:S equalize to $\sim 3:1:1$ (Table 2). We note that in all post-annealed films slight iodide-excess remains. This convergence towards the molar ratios expected from a Ag_3SI compound is in agreement with XRD (Figure 4b), where the nucleation of Ag_3SI polymorphs is observed; the $\beta\text{-Ag}_3\text{SI}$ phase being the most noticeable by its distinct peak at 31.65° .

Table 2. EDX measurements of as-deposited and annealed films. All films were deposited at room temperature, 10 Hz, a fluence of 0.75 J cm^{-2} , and a working pressure of 1.5×10^{-2} mbar. The samples were then annealed under N_2 at 200°C for 30 minutes and show a convergence of the molar ratios of the Ag:S:I to $\sim 3:1:1$, with a slight iodide excess.

	Ag	S	I
Pristine	2.69	1.53	0.78
Annealed	2.93	0.97	1.10

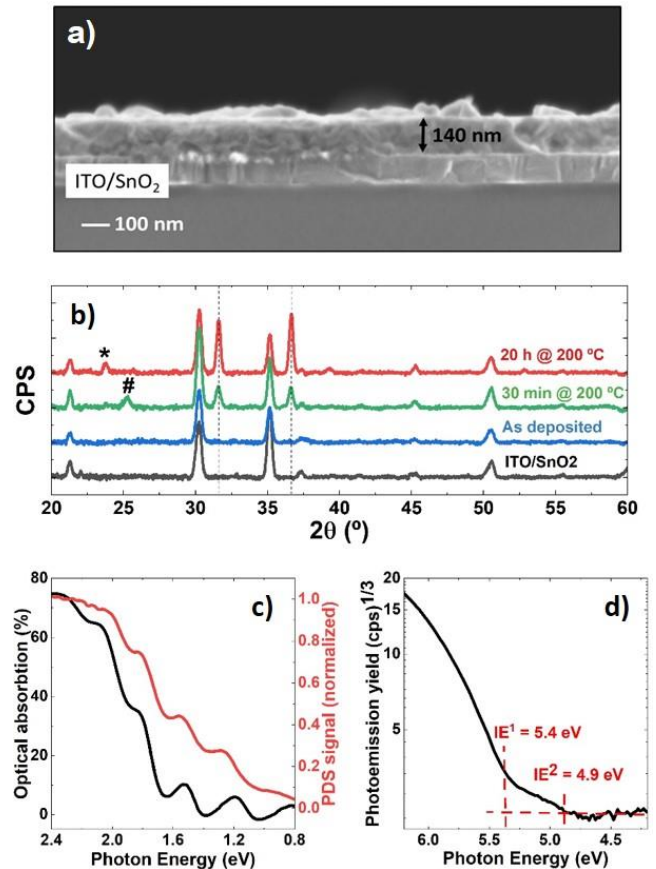


Figure 4. a) Cross-sectional SEM image of a Ag_3SI film deposited using a 3:1 S: Ag_3SI target annealed for 20 hours at 200°C . b) XRD of thin-films deposited using a sulphur-rich target of 3:1 S: Ag_3SI . These films were grown on an ITO/ SnO_2 substrate whose diffraction pattern is shown in black. Peaks from AgI and $\alpha\text{-Ag}_3\text{SI}$ phases are denoted by * and #, respectively. c) Optical and PDS spectra. d) APS characterization showing ionization energy.

Upon further annealing for 20h, antiperovskite diffraction peaks become more intense, translating an increased crystallization of amorphous material. A slight narrowing of diffraction peaks is also observed (see Figure S9) suggesting some crystallite growth and/or coalescence. The cross-sectional scanning electron microscopy (SEM) of a film deposited using a 3:1 S: Ag_3SI target and subsequently annealed at 200°C for 20 hr is shown in Figure 4a with a total thickness of 140 nm.

Optical properties of the annealed antiperovskite thin film are studied by PDS and UV-visible absorption (Figure 4c). In both cases a shallow slope is observed with multiple oscillations. These may be partly ascribed to interferences but also to structural disorder of the Ag^+ cations (see further discussion on theoretical calculations in the next section). Eventually photoelectron spectroscopy in air is car-

ried out to determine the ionization energy (valence band maximum with respect to vacuum level). A linear extrapolation of the photoemission yield in linear scale gives an ionization energy around 5.4 eV (Figure S10). However, a closer look at the signal on a logarithmic scale (Figure 4d) reveals a second ionization energy around 4.9 eV. The origin of these two levels remains unclear but could also be related to structural disorder with the coexistence of α^* and β phases as suggested by Figure 4b. Kelvin probe measurements (Figure S11) indicate a work function of 4.4 eV. Therefore, the Fermi level is calculated to be 0.5 to 1.0 eV above the valence band maximum.

In order to gain insights into the dynamics of photoexcited charge carriers in Ag_3SI thin films, we carried out transient OPTP photoconductivity spectroscopy measurements. Figure 5 shows a normalized OPTP transient measured for Ag_3SI following excitation with 2.48 eV pulses. As discussed by Wehrenfennig *et al.*,⁴⁶ the conductivity value immediately following the onset can be used to extract the effective electron-hole sum mobility in the material. This method has previously been used to extract charge-carrier mobilities for several emerging thin-film semiconductors (*e.g.*, lead halide perovskites, lead-free perovskites, and other perovskite-inspired materials).^{47,48} Assuming free charge-carrier transport, we are able to extract an effective electron-hole sum mobility value of $49 \pm 1 \text{ cm}^2\text{V}^{-1}\text{s}^{-1}$. We note that the obtained mobility rivals that of lead halide perovskites and other emerging semiconductors.^{49,50} To further analyze the lifetimes of charge carriers following excitation, OPTP photoconductivity transients was fitted with a stretched exponential model revealing a short charge-carrier lifetime of $\tau \sim 24 \text{ ps}$. Interestingly, the good fit of the stretched exponential model⁵¹ indicates the strongly dispersive nature of charge-carrier recombination processes in these thin films, which is compatible with a high level of disorder and the presence of defect-mediated recombination processes, in agreement with the observation of long and shallow absorption tails reported above.

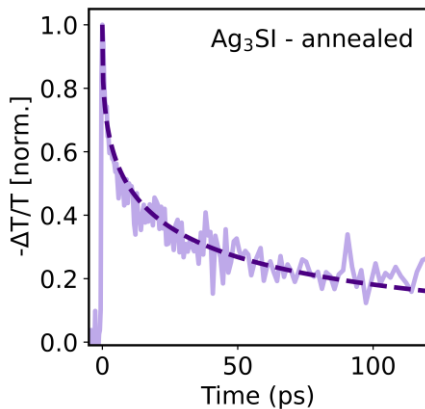


Figure 5. Normalized THz photoconductivity transient ($-\Delta T/T$) of a Ag_3SI film annealed at 200 °C recorded following excitation with 2.48 eV photons at a pulse fluence of $0.9 \mu\text{J cm}^{-2}$. The dashed line corresponds to a stretched exponential fit to the experimental data.

Having extracted the charge carrier mobility and lifetime, we estimate a charge-carrier diffusion length of $\sim 55 \text{ nm}$ using the equation $L_D = (\mu\tau k_B T/e)^{1/2}$.⁵² It is worth not-

ing that the dispersive nature of charge-carrier recombination processes in Ag_3SI this film suggests that a range of charge-carrier recombination times are present, meaning that the obtained value represents an average diffusion length value.

2.4. THEORETICAL CALCULATIONS

To shed more light into the electronic properties of these silver chalcogenide antiperovskites, especially concerning the bandgap of Ag_3SBr on which very scarce and conflicting data is available (from 0.3 to 1.9 eV),³⁴⁻³⁶ we undertook theoretical calculations at the DFT level using periodic boundary conditions (see the SI for computational details). Several phases have been previously characterized for Ag_3SI and Ag_3SBr .³² In Ag_3SBr , the β phase is the one found experimentally at room temperature, and consists of 3 Ag^+ ions distributed statistically into the 12(h) sites in a simple cubic structure with space group $Pm-3m$. Preliminary geometry optimizations indicate that the $Pm-3m$ structure where the Ag ions are placed (averaged) at the face centers is unstable (transition state), and upon small atomic displacements it evolves to a γ -like distorted structure (see Figure S12a). On the other hand, the high-temperature α phase of Ag_3SI presents random distribution of S_2^-/I^- anions, whose long-range ordering lowers the symmetry to $Pm-3m$ (β phase).⁵³ As in Ag_3SBr , upon crystal relaxation of the $Pm-3m$ cell of Ag_3SI , Ag ions move off the face center towards a $Cmcm$ -like structure (Figure S12b). Further ordering of the Ag^+ cations in one of the four equivalent Ag-positions of the β phase leads to $\gamma\text{-Ag}_3\text{SI}$ (space group $R3$).⁵³

Minimum-energy crystal structures of Ag_3SBr and Ag_3SI were obtained at the PBEsol/light tier-1 level of theory using primitive, conventional, and extended unit cells (see Figure S13). Lattice parameters for all the crystal structures are summarized in Table S3. High-level theoretical calculations using the hybrid HSE06 functional and including spin-orbit coupling (SOC) predict an indirect($T \rightarrow \Gamma$)/direct(Γ) bandgap (E_g) of 1.49/1.66 eV (Figure S14-S15), in contrast to a value of 0.88 eV reported at the less-accurate LDA level of theory,³³ but in good accord with photoacoustic experiments (1.5 and 1.85 eV for a broad absorption shoulder and peak, respectively).³⁶ The effect of the functional used in the calculations and the SOC correction on the bandgap energy is detailed in Table S4. The bandgap of Ag_3SBr is characterized by a valence-band maximum (VBM) with an even contribution of constituting Ag^+ (4d-orbitals), S^{2-} (3p-orbitals), and Br^- (4p-orbitals) ions, whereas the conduction-band minimum (CBM) mainly involves the 5s-orbital of Ag^+ (Figure 6a and S16-S17). These results therefore evidence the crucial role of Ag in the VBM/CBM nature and suggest that the Ag ordering within the crystal may influence the bandgap energy.

Enlarging the unit cell from primitive to conventional and extended orthorhombic (ORC) cells increases the Ag^+ degrees of freedom for further relaxation and symmetry alleviation, and leads to a small decrease of the bandgap to 1.42/1.58 eV (indirect/direct) and 1.44 eV, respectively (Table S4). These values are in line with the reported experimental photoacoustic data and with our powder PDS signal saturation (*ca.* 1.55 eV). The electronic band struc-

ture found for the conventional ORC unit cell of Ag_3SBr is displayed in Figure 6b, showing a large number of quasi-degenerated states below the bandgap indicative of high disorder of Ag^+ ions within the cell.

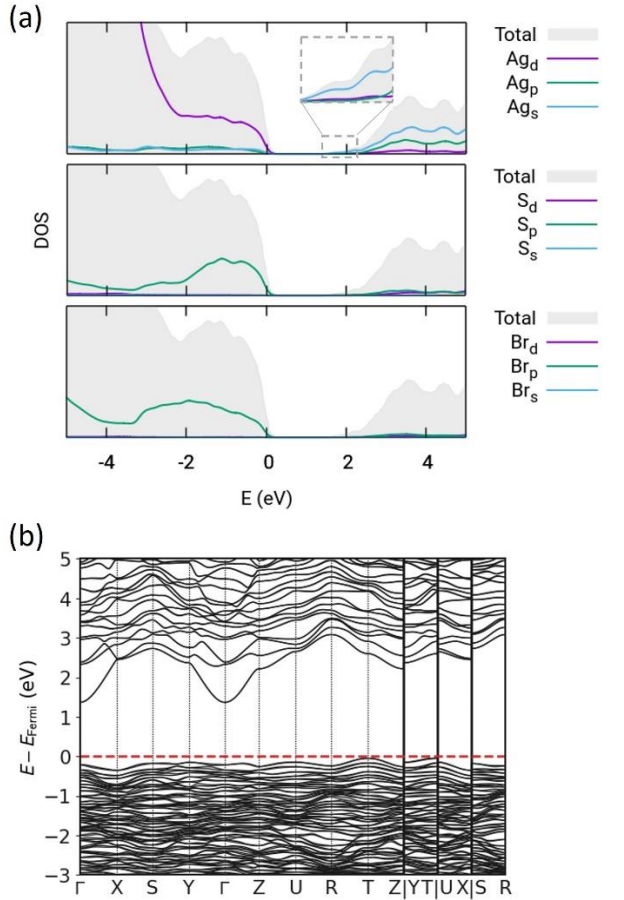


Figure 6. Mulliken orbital-projected density of states (a) and band structure (b) calculated at the HSE06+SOC level for the conventional ORC cell of Ag_3SBr .

Moving to Ag_3SI , an HSE06+SOC indirect($\text{S} \rightarrow \Gamma$)/direct(Γ) bandgap of 1.28/1.56 eV is predicted for the β -ORCC primitive cell (Figure S18-S19). For the sake of comparison, the γ phase of Ag_3SI (space group $R3$) is predicted with a bandgap of 1.34/1.71 eV for primitive rhombohedral and 1.32/1.69 eV for conventional hexagonal cells (Table S3 and Figure S13-S14). As in Ag_3SBr , Ag orbitals are highly involved in the VBM (4d-orbitals) and CBM (5s-orbital) of β - Ag_3SI (Figure S18). Moving from primitive ORCC to conventional and extended ORC cells leads to a noticeable bandgap reduction up to 0.82($\text{Z} \rightarrow \Gamma$)/1.06(Γ) and 1.00 eV, respectively (Figure S20-S23 and Table S4). This bandgap reduction is prompted by zig-zag Ag^+ ions displacements from $Cmcm$ out of ab -plane along the c -axis (Figure 7). Simulation of the absorption spectrum by means of the linear macroscopic dielectric function approximation nicely matches the PDS shape recorded experimentally for the Ag_3SI film, with several shoulders in the low-energy range (compare Figure 4c and Figure S24).

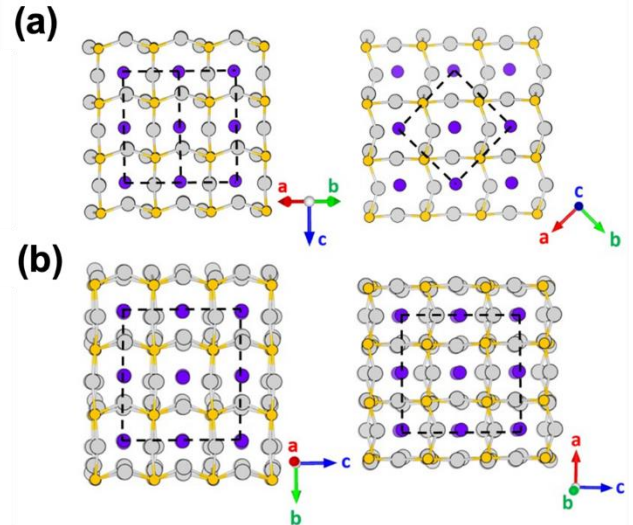


Figure 7. Minimum-energy crystal structures calculated at the PBEsol level for the primitive ORCC (a) and conventional ORC (b) unit cells of β - Ag_3SI . Color coding: gray for Ag, yellow for S, and purple for I.

On the other hand, the α^* phase of Ag_3SI was modelled by randomly exchanging 15% and 100% of the S^{2-}/I^- anions in the conventional ORC unit cell. Minimum-energy crystal structures indicate large deformations localized over the defectively positioned anions in the 15% model, whereas a fully disordered structure is predicted for 100% exchange (see Figure S25). Theoretical calculations at the HSE06+SOC level predict for α^* - Ag_3SI a significant increase in the indirect/direct bandgap from 0.82/1.06 eV (β phase) to 1.30/1.31 eV (15% random distribution) and 1.29/1.39 eV (100% random distribution), in good accordance with the experimental evidences.¹³

Finally, the thermal effect on the bandgap was disentangled by performing ab-initio Car-Parrinello molecular dynamics on Ag_3SBr and Ag_3SI for 1 ps simulation time at 300 K (see the SI for details). Theoretical calculations predict a negligible thermal effect on the bandgap of Ag_3SBr compared to the static calculations, with an average value of 1.42 ± 0.07 (indirect)/ 1.47 ± 0.08 (direct) eV. In contrast, the bandgap of Ag_3SI experiences a noticeable increase of ca. 0.3 eV during the dynamics, with an average E_g of 1.14 ± 0.14 (indirect)/ 1.38 ± 0.14 (direct) eV. In spite of this, root-mean-standard deviation (RMSD) in atomic displacements indicate that silver atoms have moved more on average in Ag_3SBr (RMSD of Ag = 1.11 Å) than in Ag_3SI (RMSD of Ag = 0.85 Å; see Table S5), suggesting that the electronic structure of the iodine-based material is more sensitive to local distortions.

3. CONCLUSIONS

In conclusion, we have shown the fast (< 2 h) and solvent-free synthesis of Ag_3SI and Ag_3SBr antiperovskites through mechanochemical synthesis and thermal annealing at moderate temperatures (160 °C and 220 °C, respectively). Thin films of Ag_3SI were successfully deposited by pulsed-laser deposition from S-enriched Ag_3SI targets. Our analysis of THz photoconductivity demonstrates that Ag_3SI

films present an excellent charge-carrier mobility of $49 \text{ cm}^2\text{V}^{-1}\text{s}^{-1}$, highlighting the potential for applications in optoelectronic devices that rely on efficient charge-carrier transport. However, the relatively fast recombination lifetimes show that development of targeted trap passivation techniques is now required in order to extend charge-carrier diffusion lengths towards the hundreds of nanometers.

ASSOCIATED CONTENT

Supporting Information.

This material is available free of charge via the Internet at <http://pubs.acs.org>.

Detailed experimental procedures, characterization methods, XRD of in-situ annealing of Ag_3SBr , XRD of hand-mixed precursors, Rietveld refinement of Ag_3SI , computed crystal structures and lattice parameters, calculated density of states, calculated band structures and bandgap energies, XRD of thin films by single- and dual-source sublimation, EDX and XRD of films by PLD, XRD of PLD targets, details of Optical-Pump-Terahertz-Probe Measurements.

AUTHOR INFORMATION

Corresponding Authors

Francisco Palazon. Instituto de Ciencia Molecular, ICMol, Universidad de Valencia, 46980 Paterna, Spain; Departamento de Ingeniería Química y Ambiental, Universidad Politécnica de Cartagena, 30202 Cartagena, Spain; <https://orcid.org/0000-0002-1503-5965>
Email: francisco.palazon@upct.es, francisco.palazon@uv.es

Henk J. Bolink. Instituto de Ciencia Molecular, ICMol, Universidad de Valencia, 46980 Paterna, Spain; <https://orcid.org/0000-0001-9784-6253>
Email: henk.bolink@uv.es

Authors

Paz Sebastia-Luna. Instituto de Ciencia Molecular, ICMol, Universidad de Valencia, 46980 Paterna, Spain; <https://orcid.org/0000-0001-6992-199X>

Nathan Rodkey. Instituto de Ciencia Molecular, ICMol, Universidad de Valencia, 46980 Paterna, Spain; MESA+ Institute for Nanotechnology, University of Twente, Enschede 7500 AE, The Netherlands; <https://orcid.org/0000-0003-4246-3911>

Adeem Saeed Mirza. MESA+ Institute for Nanotechnology, University of Twente, Enschede 7500 AE, The Netherlands <https://orcid.org/0000-0003-1217-6858>

Sigurd Mertens. Institute for Materials Research (IMO-IMOMECE), Hasselt University, Diepenbeek BE – 3590, Belgium.

Snigdha Lal. Department of Physics, University of Oxford, Clarendon Laboratory, Parks Road, Oxford OX1 3PU, UK.

Axel M. Gaona-Carranza. Instituto de Ciencia Molecular, Universidad de Valencia, 46980 Paterna, Spain; <https://orcid.org/0000-0001-5911-1512>

Joaquín Calbo. Instituto de Ciencia Molecular, Universidad de Valencia, 46980 Paterna, Spain; <https://orcid.org/0000-0003-4729-0757>

Marcello Righetto. Department of Physics, University of Oxford, Clarendon Laboratory, Parks Road, Oxford OX1 3PU, UK.

Michele Sessolo. Instituto de Ciencia Molecular, Universidad de Valencia, 46980 Paterna, Spain.

Laura M. Herz. Department of Physics, University of Oxford, Clarendon Laboratory, Parks Road, Oxford OX1 3PU, UK, Institute for Advanced Study, Technical University of Munich, Lichtenbergstrasse 2a, D-85748 Garching, Germany.

Koen Vandewal. Institute for Materials Research (IMO-IMOMECE), Hasselt University, Diepenbeek BE – 3590, Belgium; <https://orcid.org/0000-0001-5471-383X>

Enrique Ortí. Instituto de Ciencia Molecular, Universidad de Valencia, 46980 Paterna, Spain; <https://orcid.org/0000-0001-9544-8286>

Mónica Morales-Masis. MESA+ Institute for Nanotechnology, University of Twente, Enschede 7500 AE, The Netherlands; <https://orcid.org/0000-0003-0390-6839>

Author Contributions

The manuscript was written through contributions of all authors.

Notes

The authors declare no competing financial interest.

ACKNOWLEDGMENT

The research leading to these results has received funding from the European Research Council (ERC) under the European Union's Horizon 2020 research and innovation programme (grant agreement No. 834431). Authors acknowledge support from the Comunitat Valenciana (IDIFEDER/2018/061, GV/2021/027 and PROMETEU/2020/077), as well as by the Ministry of Science and Innovation (MCIN) and the Spanish State Research Agency (AEI) (projects PCI2019-111829-2, PID2020-119748GA-I00, PID2021-128569NB-I00, and CEX2019-000919-M, funded by MCIN/AEI/10.13039/501100011033 and by “ERDF A way of making Europe”, and project TED2021-131255B-C44 funded by MCIN/AEI/10.13039/501100011033 and by European Union NextGenerationEU/PRTR). Dutch Research Council (NWO, FOM Focus Group “Next Generation Organic Photovoltaics”). P. S. thanks the Spanish Ministry of Universities for her predoctoral grant (FPU18/01732 and EST19/00295). F. P. acknowledges funding from the Ramón y Cajal program of the Spanish Ministry of Science (RYC2020-028803-I). ASM and MMM acknowledge the financial support of the NWO StartUp 2019 project BRIDGE (project number: STU.019.026). M.R and L.M.H acknowledge financial support from the Engineering and Physical Sciences Research Council UK.

REFERENCES

- (1) Akkerman, Q. A.; Manna, L. What Defines a Halide Perovskite? *ACS Energy Lett.* **2020**, 604–610.
- (2) Wells, H. L. Über Die Cäsium- Und Kalium- Bleihalogenide. *Zeitschrift für Anorg. und Allg. Chemie* **1893**, 3 (1), 195–210.

- (3) Reuter, B.; Hardel, K. Silbersulfidbromid Und Silbersulfidjodid. *Angew. Chemie* **1960**, *72* (4), 138–139.
- (4) Chiodelli, G.; Magistris, A.; Schiraldi, A. Ag₃SBr and Ag₃SI: Ionic Conductivity of Their Modifications in the Range 93–573 K. *Zeitschrift für Phys. Chemie Neue Folge* **1979**, *118*, 177–186.
- (5) Spinolo, G.; Massarotti, V. Ag₃SBr and Ag₃SI a Diffractometric Study of the Low Temperature Modifications. *Zeitschrift für Phys. Chemie* **1980**, *121* (1), 7–15.
- (6) Kawamura, J.; Siitmoji, M.; Hoshino, H. The Ionic Conductivity and Thermoelectric Power of the Superionic Conductor Ag₃SBr. *J. Phys. Soc. Japan* **1981**, *50* (1), 194–200.
- (7) Kennedy, J. H.; Chen, F. Solid Electrolyte Coulometry. Silver Sulfide Bromide Electrolyte. *Electrochem Soc-J* **1969**, *116* (2), 207–211.
- (8) Magistris, A.; Chiodelli, G.; Schiraldi, A. Low Temperature Phase Transitions of Ag₃SBr and Ag₃SI. *Zeitschrift für Phys. Chemie* **1978**, *112* (2), 251–253.
- (9) Reuter, B.; Hardel, K. Silbersulfidbromid Ag₃SBr Und Silbersulfidjodid Ag₃SI. II. Die Kristallstrukturen von Ag₃SBr, B- Und A-Ag₃SI. *ZAAC - Zeitschrift für Anorg. und Allg. Chemie* **1965**, *340* (3–4), 168–180.
- (10) Reuter, B.; Hardel, K. Über Die Hochtemperaturmodifikation von Silbersulfidjodid. *Kurze Orig.* **1961**, *48*, 161.
- (11) Kurita, M.; Nakagawa, K.; Wakamura, K. Fundamental Absorption Edge of α-AgI-Type Superionic Conductor Ag₃SBr. *Japanese J. Appl. Physics, Part 1 Regul. Pap. Short Notes Rev. Pap.* **2000**, *39* (4 A), 1786–1787.
- (12) Xianglian, H. H.; Basar, K.; Siagian, S.; Sakuma, T.; Takahashi, H.; Tubuqinbaer; Kawaji, H.; Atake, T. Low-Temperature Phase in Superionic Conductor Ag₃SBr XI 1-X. *J. Phys. Soc. Japan* **2007**, *76* (11), 3–6.
- (13) Kurita, M.; Nakagawa, K.; Akao, F. Photoacoustic Spectrum in Superionic Conductors Ag₃SI and AgI. *Jpn. J. Appl. Phys.* **1988**, *27* (10 A), L1920–L1922.
- (14) Takahashi, T.; Yamamoto, O. The Ag/Ag₃SI/I₂ Solid-Electrolyte Cell. *Electrochim. Acta* **1966**, *11* (7), 779–789.
- (15) Hoshino, S.; Sakuma, T.; Fujii, Y. A Structural Phase Transition in Superionic Conductor Ag₃SI. *J. Phys. Soc. Japan* **1979**, *47* (4), 1252–1259.
- (16) Hoshino, S.; Fujishita, H.; Takashige, M.; Sakuma, T. Phase Transition of Ag₃SX (X=I, Br). *Solid State Ionics* **1981**, *3–4* (C), 35–39.
- (17) Yin, L.; Murphy, M.; Kim, K.; Hu, L.; Cabana, J.; Siegel, D. J.; Lapidus, S. H. Synthesis of Antiperovskite Solid Electrolytes: Comparing Li₃SI, Na₃SI, and Ag₃SI. *Inorg. Chem.* **2020**, *59* (16), 11244–11247.
- (18) Hull, S.; Keen, D. A.; Gardner, N. J. G.; Hayes, W. The Crystal Structures of Superionic Ag₃SI. *J. Phys. Condens. Matter* **2001**, *13* (10), 2295–2316.
- (19) Tver'yanovich, Y. S.; Bal'makov, M. D.; Tomaev, V. V.; Borisov, E. N.; Volobueva, O. Ion-Conducting Multilayer Films Based on Alternating Nanolayers Ag₃SI, AgI and Ag₂S, AgI. *Glas. Phys. Chem.* **2008**, *34* (2), 150–154.
- (20) Kojima, A.; Hoshino, S.; Noda, Y.; Fujii, K.; Kanashiro, T. Modified Bridgman Growth of Centimeter-Large Single Crystals of the Solid Electrolyte Ag₃SI. *J. Cryst. Growth* **1989**, *94* (2), 293–298.
- (21) Wakamura, K.; Miura, F.; Kojima, A.; Kanashiro, T. Observation of Anomalously Increasing Phonon Damping Constant in the Phase of the Fast-Ionic Conductor Ag₃SI. *Phys. Rev. B* **1990**, *41* (5), 2758–2762.
- (22) Beeken, R. B.; Wright, T. J.; Sakuma, T. Effect of Chloride Substitution in the Fast Ion Conductor Ag₃SBr. *J. Appl. Phys.* **1999**, *85* (11), 7635–7638.
- (23) Beeken, R. B.; Beeken, E. M. Ionic Conductivity in Cu-Substituted Ag₃SBr. *Solid State Ionics* **2000**, *136–137*, 463–467.
- (24) Beeken, R. B.; Jetzer, W. L.; Smith, D. R. Ionic Conduction in Cd-Substituted Ag₃SBr. *Solid State Ionics* **1994**, *70/71*, 176–179.
- (25) Beeken, R. B.; Haase, A. T.; Hoerman, B. H.; Klawikowski, S. J. The Effect of Non-Stoichiometry in Ag₃SBr. *Solid State Ionics* **1998**, *113–115*, 509–513.
- (26) Yan, S.; Xiao, H.; Liu, X. Rapid Fabrication and Thermal Performance of Ag₃Si Super-Ionic Conductor. *Chalcogenide Lett.* **2016**, *13* (10), 483–487.
- (27) Huber, H.; Mali, M.; Roos, J.; Brinkmann, D. Test of Diffusion Models for the Superionic Conductor -Ag₃SBr by Silver NMR at 1 Bar and 7 Kbar. *Phys. Rev. B* **1988**, *37* (4), 1441–1447.
- (28) Huber, H.; Mali, M.; Roos, J.; Brinkmann, D. Diffusion and Pressure Effects in the Superionic Conductor Ag₃SBr Studied by NMR. *Solid State Ionics* **1986**, *18–19* (PART 2), 1188–1192.
- (29) Huber, H.; Mali, M.; Roos, J.; Brinkmann, D. NMR Relaxation at Pressures up to 7 Kbar in the Superionic Conductor Ag₃SBr. *Phys. B+C* **1986**, *139–140* (C), 289–291.
- (30) Gras, B.; Funke, K. Non-Periodic Local Motion of Silver Ions in β-Ag₃SI from Far-Infrared Conductivity Measurements. *Solid State Ionics* **1981**, 341–346.
- (31) Yin, L.; Murphy, M.; Kim, K.; Hu, L.; Cabana, J.; Siegel, D. J.; Lapidus, S. H. Synthesis of Antiperovskite Solid Electrolytes: Comparing Li₃SI, Na₃SI, and Ag₃SI. *Inorg. Chem.* **2020**, *59* (16), 11244–11247.
- (32) Sakuma, T.; Hoshino, S. The Phase Transition and the Structures of Superionic Conductor Ag₃SBr. *J. Phys. Soc. Japan* **1980**, *49* (2), 678–683.
- (33) Shimosaka, W.; Kashida, S.; Kobayashi, M. Electronic Structure of Ag₃SI. *Solid State Ionics* **2005**, *176* (3–4), 349–355.
- (34) Materials Project. Ag₃SBr - mp-1105645.
- (35) Materials Project. Ag₃SI - mp-558189.
- (36) Kurita, M.; Nakagawa, K.; Wakamura, K. Fundamental Absorption Edge of α-AgI-Type Superionic Conductor Ag₃SBr. *Japanese J. Appl. Physics, Part 1 Regul. Pap. Short Notes Rev. Pap.* **2000**, *39* (4 A), 1786–1787.
- (37) Palazon, F.; Ajjour, Y. El; Bolink, H. J. Making by Grinding: Mechanochemistry Boosts the Development of Halide Perovskites and Other Multinary Metal Halides. *Adv. Energy Mater.* **2019**, *1902499*, 1–13.
- (38) Jackson, W. B.; Amer, N. M.; Boccara, A. C.; Fournier, D. Photothermal Deflection Spectroscopy and Detection. *Appl. Opt.* **1981**, *20* (8), 1333–1344.
- (39) Gokmen, T.; Gunawan, O.; Todorov, T. K.; Mitzi, D. B. Band Tailing and Efficiency Limitation in Kesterite Solar Cells. *Appl. Phys. Lett.* **2013**, *103506*.
- (40) Rey, G.; Larramona, G.; Bourdais, S.; Choné, C.; Delatouche, B.; Jacob, A.; Dennler, G.; Siebentritt, S. On the Origin of Band-Tails in Kesterite. *Sol. Energy Mater. Sol. Cells* **2017**, No. November, 1–10.
- (41) Wang, Y.; Kavanagh, S. R.; Burgués-Ceballos, I.; Walsh, A.; Scanlon, D. O.; Konstantatos, G. Cation Disorder Engineering Yields AgBiS₂ Nanocrystals with Enhanced Optical Absorption for Efficient Ultrathin Solar Cells. *Nat. Photonics* **2022**, *16*, 235–241.
- (42) Momblona, C.; Gil-Escrig, L.; Bandiello, E.; Hutter, E. M.; Sessolo, M.; Lederer, K.; Blochwitz-Nimoth, J.; Bolink, H. J. Efficient Vacuum Deposited P-i-n and n-i-p Perovskite Solar Cells Employing Doped Charge Transport Layers. *Energy Environ. Sci.* **2016**, *9* (11), 3456–3463.
- (43) Choi, H.; Jeong, J.; Kim, H. B.; Kim, S.; Walker, B.; Kim, G. H.; Kim, J. Y. Cesium-Doped Methylammonium Lead Iodide Perovskite Light Absorber for Hybrid Solar Cells. *Nano*

Energy **2014**, *7*, 80–85.

- (44) El Ajjouri, Y.; Palazon, F.; Sessolo, M.; Bolink, H. J. Single-Source Vacuum Deposition of Mechanothesized Inorganic Halide Perovskites. *Chem. Mater.* **2018**, *30*, 7423–7427.
- (45) Rodkey, N.; Kaal, S.; Sebastia-Luna, P.; Birkhölzer, Y. A.; Ledinsky, M.; Palazon, F.; Bolink, H. J.; Morales-Masis, M. Pulsed Laser Deposition of Cs₂AgBiBr₆: From Mechanochemically Synthesized Powders to Dry, Single-Step Deposition. *Chem. Mater.* **2021**, *33* (18), 7417–7422.
- (46) Wehrenfennig, C.; Eperon, G. E.; Johnston, M. B.; Snaith, H. J.; Herz, L. M. High Charge Carrier Mobilities and Lifetimes in Organolead Trihalide Perovskites. **2014**, 1584–1589.
- (47) Buizza, L. R. V.; Sansom, H. C.; Wright, A. D.; Ulatowski, A. M.; Johnston, M. B.; Snaith, H. J.; Herz, L. M. Interplay of Structure, Charge-Carrier Localization and Dynamics in Copper-Silver-Bismuth-Halide Semiconductors.
- (48) Jia, Z.; Righetto, M.; Yang, Y.; Xia, C. Q.; Li, Y.; Li, R.; Li, Y.; Yu, B.; Liu, Y.; Huang, H.; et al. Charge-Carrier Dynamics of Solution-Processed Antimony- and Bismuth-Based Chalcogenide Thin Films. *ACS Energy Lett.* **2023**, *8* (3), 1485–1492.
- (49) Kober-Czerny, M.; Motti, S. G.; Holzhey, P.; Wenger, B.; Lim, J.; Herz, L. M.; Snaith, H. J. Excellent Long-Range Charge-Carrier Mobility in 2D Perovskites. *Adv. Funct. Mater.* **2022**, *32* (36).
- (50) Herz, L. M. Charge-Carrier Mobilities in Metal Halide Perovskites: Fundamental Mechanisms and Limits. *ACS Energy Lett.* **2017**, *2* (7), 1539–1548.
- (51) Johnston, D. C. Stretched Exponential Relaxation Arising from a Continuous Sum of Exponential Decays. *Phys. Rev. B - Condens. Matter Mater. Phys.* **2006**, *74* (18), 1–7.
- (52) Buizza, L. R. V.; Crothers, T. W.; Wang, Z.; Patel, J. B.; Milot, R. L.; Snaith, H. J.; Johnston, M. B.; Herz, L. M. Charge-Carrier Dynamics, Mobilities, and Diffusion Lengths of 2D–3D Hybrid Butylammonium–Cesium–Formamidinium Lead Halide Perovskites. *Adv. Funct. Mater.* **2019**, *29* (35).
- (53) Hull, S.; Keen, D. A.; Gardner, N. J. G.; Hayes, W. The Crystal Structures of Superionic Ag₃SI. *J. Phys. Condens. Matter* **2001**, *13* (10), 2295–2316.

Authors are required to submit a graphic entry for the Table of Contents (TOC) that, in conjunction with the manuscript title, should give the reader a representative idea of one of the following: A key structure, reaction, equation, concept, or theorem, etc., that is discussed in the manuscript. Consult the journal's Instructions for Authors for TOC graphic specifications.

Insert Table of Contents artwork here
